

Diffusion-empowered AutoPrompt MedSAM

Peng Huang, Shu Hu, Bo Peng, Jiashu Zhang, Hongtu Zhu, *Fellow, IEEE*, Xi Wu, and Xin Wang, *Senior Member, IEEE*

Abstract—MedSAM, a medical foundation model derived from the SAM architecture, has demonstrated notable success across diverse medical domains. However, its clinical application faces two major challenges: the dependency on labor-intensive manual prompt generation, which imposes a significant burden on clinicians, and the absence of semantic labeling in the generated segmentation masks for organs or lesions, limiting its practicality for non-expert users. To address these limitations, we propose AutoMedSAM, an end-to-end framework derived from SAM, designed to enhance usability and segmentation performance. AutoMedSAM retains MedSAM’s image encoder and mask decoder structure while introducing a novel diffusion-based class prompt encoder. The diffusion-based encoder employs a dual-decoder structure to collaboratively generate prompt embeddings guided by sparse and dense prompt definitions. These embeddings enhance the model’s ability to understand and process clinical imagery autonomously. With this encoder, AutoMedSAM leverages class prompts to embed semantic information into the model’s predictions, transforming MedSAM’s semi-automated pipeline into a fully automated workflow. Furthermore, AutoMedSAM employs an uncertainty-aware joint optimization strategy during training to effectively inherit MedSAM’s pre-trained knowledge while improving generalization by integrating multiple loss functions. Experimental results across diverse datasets demonstrate that AutoMedSAM achieves superior performance while broadening its applicability to both clinical settings and non-expert users. Code is available at <https://github.com/HP-ML/AutoPromptMedSAM.git>.

Index Terms—MedSAM, medical image foundation model, end-to-end, diffusion model, uncertainty learning

I. INTRODUCTION

DEEP learning models have traditionally been applied in medicine by designing and training specialized models for specific tasks, achieving significant success [1]–[4]. However, these approaches often require training model from scratch using corresponding data [5]–[7], leading to low training efficiency and limited transferability to other tasks [8],

Peng Huang, Bo Peng, and Jiashu Zhang are with the School of Computing and Artificial Intelligence, Southwest Jiaotong University, Chengdu, China (e-mail: huangpeng@my.swjtu.edu.cn; bpeng@swjtu.edu.cn; jszhang@swjtu.edu.cn).

Shu Hu is with the Department of Computer and Information Technology, Purdue University, USA (e-mail: hu968@purdue.edu).

Hongtu Zhu is with the University of North Carolina at Chapel Hill, USA (e-mail: htzhu@email.unc.edu).

Xi Wu is with the School of Computer Science, Chengdu University of Information Technology, Chengdu, China (e-mail: wuxi@cuit.edu.cn).

Xin Wang is with the College of Integrated Health Sciences and the AI Plus Institute, University at Albany, State University of New York, USA (e-mail: xwang56@albany.edu).

Corresponding Author: Jiashu Zhang, Xin Wang.

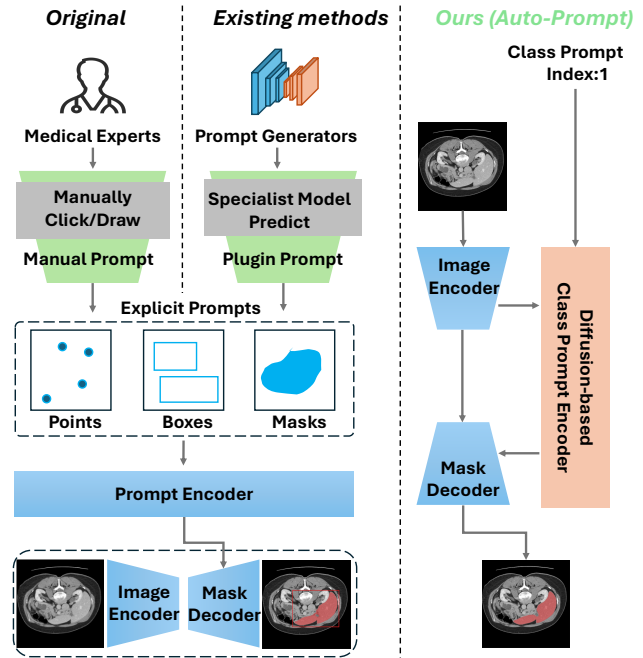


Fig. 1. Comparison with SAM-based models. (Left) The original SAM model relies on manual prompts from medical experts, restricting its usability and scenarios. (Middle) Current SAM-based methods employ specialist models for prompt generation, but these models are organ- or lesion-specific, limiting SAM’s generalizability. (Right) Our method introduces an automatic diffusion-based class prompt encoder, removing the need for explicit prompts, adding semantic labels to masks, and enabling accurate, end-to-end segmentation for non-experts in diverse medical contexts.

[9]. Recently, prompt-based foundational models in computer vision, such as the Segment Anything Model (SAM) [10], have demonstrated impressive performance and generalization capabilities in various semantic segmentation tasks based on user-provided prompts [11], [12].

Compared to natural images, medical images generally have lower contrast, lower resolution, and high inter-class similarity, with strong domain-specific characteristics. As a result, SAM performs poorly in the medical domain. To address this, Ma et al. proposed the foundational medical model MedSAM [13], which has been optimized for the unique characteristics of medical images. In its optimization process, MedSAM utilized over one million medical masks, including common modalities such as MRI and CT, marking the entry of segmentation models in the medical field into the era of large segmentation models.

Although MedSAM boasts impressive zero-shot and few-shot segmentation capabilities, it is essentially a fine-tuned version of SAM without changes to its prompt-based framework. This means that MedSAM retains both the advantages and shortcomings of SAM [10], [14]. Specifically: **(1) Dependency on Manual Prompts:** It requires users to provide precise prompts to segment the target region. However, creating prompts for medical images requires expertise, and in clinical settings, providing explicit prompts like points, bounding boxes, or scribbles is impractical. **(2) Prompt Encoder Limitations:** The Prompt Encoder limits MedSAM’s segmentation capabilities. The manual nature of these prompts means the error may not be within a controllable range [15]. Using the bounding box prompt as an example, MedSAM’s performance relies on the discrepancy between the prompt box and the true boundary. However, other targets within the prompt box cannot be avoided, and different organ or lesion categories often exhibit high similarity and low inter-class variation [16]. **(3) Lack of Semantic Information:** MedSAM cannot obtain the semantic information of the masks it predicts. It can only predict binary masks for each prompt, without associating them with semantic labels [10], [13], [17].

To address these challenges, we propose AutoMedSAM. A comparison between AutoMedSAM and existing methods is shown in Fig. 1. We replaced the original prompt encoder with a diffusion-based class prompt encoder. This new encoder uses lesion or organ index as a prompt, incorporating semantic information about the target into the AutoMedSAM learning process. The class prompts and image embeddings are input information to generate prompt embeddings for the mask decoder directly. By generating prompt embeddings directly from class prompts, we eliminate the robustness issues caused by manually provided explicit prompts and transform the semi-automatic MedSAM into a fully automated end-to-end process. Meanwhile, we designed an uncertainty-aware joint optimization training strategy. This strategy can optimize the model training process by combining the advantages of multiple loss functions while transferring the pre-training knowledge from MedSAM to AutoMedSAM. This enables AutoMedSAM to adapt to data of various modalities and effectively extract features of different organs or lesions, enhancing the segmentation performance and robustness of the model.

In summary, our contributions are as follows:

- 1) We introduced AutoMedSAM, which overcomes the limitations of the prompt-based SAM with a novel architecture, expanding the model’s applicability to a broader range of users and scenarios. This method is adaptable to more medical contexts and, through an end-to-end workflow, enables non-medical experts to obtain accurate segmentation results without relying on manual prompts.
- 2) We propose a diffusion-based class prompt encoder that eliminates the need for explicit prompts while adding semantic labels to the predicted masks. During the diffusion process, the class prompt is projected, allowing the model to capture class-specific features better. The unique two-decoder structure, combined with the definitions of sparse and dense prompt embeddings,

enhances the controllability of the generation process.

- 3) We designed an uncertainty-aware joint optimization method that efficiently transfers the pre-trained knowledge from MedSAM to AutoMedSAM, while dynamically leveraging multiple loss functions to enhance the model’s generalization ability across multi-modal data.

II. RELATED WORKS

A. SAM-based Medical Image Segmentation

SAM represents a significant breakthrough in transforming image segmentation from specialized applications to a general-purpose tool [18]. Its extensive pretraining on large-scale data has endowed it with remarkable zero-shot generalization capabilities [19]. Research on SAM-based medical image segmentation can be broadly divided into two categories. The first category focuses on fine-tuning while retaining the manual prompt structure to enhance performance. MedSAM was trained with a large volume of medical data to create a medical version of SAM [13]. MedSAM employs the EfficientViT model to replace the image encoder in SAM and improves the performance of the model after fine-tuning it on multimodal data [20]. However, manual prompts are difficult to provide accurately in clinical settings [16], leading to a second category of research focusing on replacing manual prompts to make SAM a fully automated process, as seen in models like MaskSAM and UV-SAM [17], [21]. These approaches introduce additional models to generate rough masks, but the added structures are often task-specific, making the SAM model more cumbersome. Adaptive SAM and SP-SAM utilize CLIP to encode textual prompts into prompt embeddings [22], [23]. Although these methods achieve a fully automated segmentation process, they still rely on prompts, leaving the issues outlined in Section I unresolved. Our proposed AutoMedSAM not only eliminates the need for manual prompts but also fully taps into SAM’s inherent potential. Moreover, the class prompt encoder can be extended to all SAM-based foundational models.

B. Diffusion Models for Medical

Diffusion models show strong potential in medical imaging, achieving notable success in tasks such as image generation, segmentation, and classification [24]–[26]. The initial applications of diffusion models in the medical field primarily focused on generating medical data, which has proven useful for medical data augmentation [27]. In addition, several scholars have investigated the potential of medical images generated by diffusion models as a substitute for real data in training deep networks. M. Usman Akbar et al. and D. Stojanovski et al. demonstrated that these synthetic data are effective for downstream tasks [28], [29]. Recent studies have used diffusion models for cross-modality synthesis [30], [31]. For example, DCE-diff addresses data heterogeneity by leveraging multimodal non-contrast images to extract anatomical details from structural MRI sequences and perfusion information from ADC images, enabling the synthesis of early- and late-phase DCE-MRI [32]. D. Stojanovski et al. demonstrated that visual realism during model training does not necessarily

correlate with model performance. Consequently, these models can generate organ or lesion features optimized for deep learning, thereby enhancing the accuracy of downstream tasks. Furthermore, utilizing more efficient models can significantly reduce computational costs [29].

III. METHOD

A. Overview of AutoMedSAM

The optimization of AutoMedSAM is essentially based on the structure of SAM, with the innovative introduction of a diffusion-based class prompt encoder to address the challenges of manual prompts. Specifically, as illustrated in Fig. 2, AutoMedSAM consists of three core modules: an image encoder E_I , a diffusion-based class prompt encoder E_P , and a mask decoder D_M . The input image is denoted as $I \in \mathbb{R}^{h \times w \times 3}$, with spatial resolution $h \times w$. By providing the prompt class c , AutoMedSAM can predict the mask corresponding to the class c . The image is first processed by the image encoder to generate image embedding F_I . Subsequently, the class prompt encoder E_P , based on a diffusion model, processes the image embedding to generate sparse prompt embedding $P_s^{(c)}$ and dense prompt embedding $P_d^{(c)}$ from the target prompts. Finally, the mask decoder combines the image embedding, positional encoding P_p , sparse prompt embedding, and dense prompt embedding to predict the segmentation mask $M^{(c)}$ for class c . The entire process can be represented as:

$$F_I = E_I(I), \quad (1a)$$

$$P_s^{(c)}, P_d^{(c)} = E_P(F_I, c), \quad (1b)$$

$$M^{(c)} = D_M(F_I, P_p, P_s^{(c)}, P_d^{(c)}). \quad (1c)$$

B. Diffusion-based Class Prompt Encoder

Through an exploration of the SAM mechanism, we found that the goal of the prompt encoder is to generate sparse and dense prompt embeddings. To eliminate the need for manual prompts, we propose a diffusion-based class prompt encoder that integrates the diffusion process with an encoder-decoder framework. Fig. 3 shows the detailed network structure. As seen, it consists of an encoder and two decoders. The two decoder branches are tasked with generating sparse and dense prompt embeddings, respectively. Additionally, the class prompt not only guides the entire generation process but also ensures that the model's prediction masks carry semantic information.

1) *Forward Conditional Generation Diffusion*: In the forward diffusion process, the prompt class c is projected and integrated into the noise generation process, enabling the image embeddings to incorporate class information at each step of the diffusion. This approach helps enhance the model's ability to capture class-specific features when processing inputs with distinct class attributes. Specifically, the class prompt is projected through a linear layer to match the dimensions of the image embedding. The projection process can be represented as:

$$c_{\text{proj}} = W_c c + b_c, \quad (2)$$

where $W_c \in \mathbb{R}^{H \times W}$ and $b_c \in \mathbb{R}^{H \times W}$ are the weight matrix and bias vector of the linear layer. The projected class prompt c_{proj} is then reshaped to:

$$c_{\text{expand}} = c_{\text{proj}} \cdot \text{view}(B, 1, H, W) \in \mathbb{R}^{B \times 1 \times H \times W}. \quad (3)$$

At each time step t , the generated Gaussian noise ϵ_t follows a normal distribution with zero mean and variance σ_t^2 :

$$\epsilon_t \sim \mathcal{N}(0, \sigma_t^2), \quad \sigma_t = \frac{1}{t+1} \quad (4)$$

As the time step t increases, the noise scale gradually decreases. Finally, the forward diffused embedding F_t is obtained by adding the image embedding F_I , the projected class prompt c_{expand} , and the Gaussian noise ϵ_t together:

$$F_t = F_I + \epsilon_t + c_{\text{expand}}. \quad (5)$$

By conditional generation, we integrate class information into the noise generation process, making the forward diffusion process conditional rather than unconditional. This enhances the controllability of the generation process. This approach enhances feature representation quality and strengthens the model's ability to differentiate class-specific features, thereby improving prompt embedding generation performance.

2) *Two-branch Reverse Diffusion*: In SAM, dense prompt embeddings capture fine-grained local information specific to a target, while sparse prompt embeddings emphasize capturing broader global features. To distinguish the functional roles of the two embedding types, our diffusion-based class prompt encoder incorporates a single encoder with two independent decoder branches [33], designed to analyze local and global features and produce distinct prompt embeddings. Based on the specific use of dense and sparse prompt embeddings, element-wise attention is applied to the dense prompt branch, while channel-wise attention is used for the sparse prompt branch. Additionally, the model employs skip connections between the encoder and decoder to retain low-level features [34]. During this process, the prompt class c is encoded and combined with embeddings from the encoder, enabling the model to focus on input features relevant to the specific category more effectively. This enhances the model's ability to perceive and distinguish category-specific features, thereby improving the quality and specificity of the generation process.

Specifically, the diffusion embedding $F_t \in \mathbb{R}^{B \times C \times H \times W}$ obtained from forward diffusion is fed into the encoder, which captures its features progressively. The encoding process can be represented as:

$$F_{\text{enc}}^{(l)} = \sigma(W^{(l)} * F_{\text{enc}}^{(l-1)} + b^{(l)}), \quad \forall l = 1, 2, \dots, L \quad (6)$$

where $F_{\text{enc}}^{(l)}$ is the output feature at layer l , $F_{\text{enc}}^{(0)} = F_t$ represents the diffusion embedding, $W^{(l)}$ is the weight matrix of the convolution kernel, $b^{(l)}$ is the bias vector, $*$ denotes the convolution operation, and σ represents the ReLU activation function.

After obtaining the encoder's output feature $F_{\text{enc}}^{(l)}$, we code the class prompt c via (2) and (3) to align with the feature map's dimensions. Subsequently, we concatenate $F_{\text{enc}}^{(l)}$ with the post-coding prompt c_p along the channel dimension. The concatenated feature $F_{\text{att}}^{(l)}$ contains the image information of

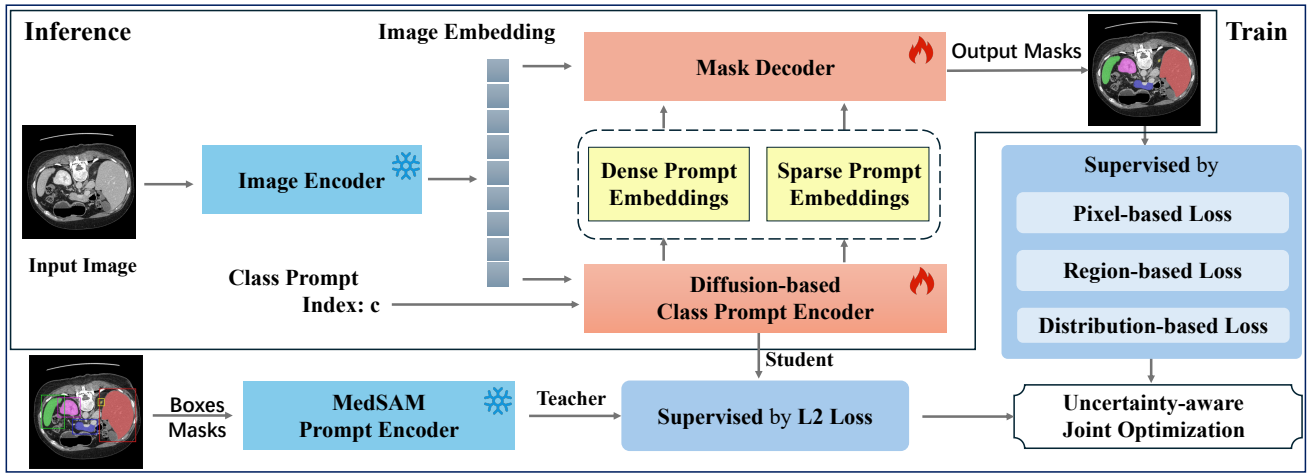


Fig. 2. An overview of the AutoMedSAM. AutoMedSAM generates dense and sparse prompt embeddings through a diffusion-based class prompt encoder, eliminating the need for explicit prompts. During training, we employ an uncertainty-aware joint optimization strategy with multiple loss functions for supervision, while transferring MedSAM’s pre-trained knowledge to AutoMedSAM. This approach improves training efficiency and generalization. With end-to-end inference, AutoMedSAM overcomes SAM’s limitations, enhancing usability and expanding its application scope and user base.

the prompt class. It is then passed through the dense prompt embedding branch and the sparse prompt embedding branch separately:

Dense Prompt Embedding Branch. To refine the exploration of local features, we compute the attention weights $A_{\text{dense}}^{(l)}$ using an element-wise convolution operation:

$$A_{\text{dense}}^{(l)} = \sigma(W_{\text{att}}^{(l)} * F_{\text{att}}^{(l)} + b_{\text{att}}^{(l)}). \quad (7)$$

Next, we apply these attention weights to $F_{\text{enc}}^{(l)}$, automatically focusing on the fine-grained features related to the prompt.

$$F_{\text{dense}}^{(l)'} = F_{\text{enc}}^{(l)} \odot A_{\text{dense}}^{(l)}, \quad (8)$$

where \odot denotes element-wise multiplication. The resulting attention-enhanced feature $F_{\text{enc}}^{(l)'}$ is subsequently concatenated with the corresponding feature from the skip connection and provided as input to the decoder for progressive layer-by-layer decoding:

$$P_d^{(c)} = F_{\text{dec}}^{(l-1)} = \sigma(W_{\text{dec}}^{(l)} * F_{\text{dec}}^{(l)} + b_{\text{dec}}^{(l)}). \quad (9)$$

The $P_d^{(c)}$ obtained from the dense branch contains rich features related to the prompt.

Sparse Prompt Embedding Branch. The sparse prompt embedding necessitates the branch to develop a deeper understanding of global information. To achieve this, we perform global adaptive average pooling on the information from each channel for compression, yielding the global feature $F_{\text{global}}^{(l)}$:

$$F_{\text{global}}^{(l)} = \text{AdaptiveAvgPool2D}(F_{\text{att}}^{(l)}). \quad (10)$$

We then determine the channel attention weights $A_{\text{sparse}}^{(l)}$ via *Sigmoid* :

$$A_{\text{sparse}}^{(l)} = \text{Sigmoid}(W_{\text{att}}^{(l)} * F_{\text{global}}^{(l)} + b_{\text{att}}^{(l)}). \quad (11)$$

The obtained channel attention weights are subsequently applied to the encoder’s output feature to enhance globally

relevant class information:

$$F_{\text{sparse}}^{(l)'} = F_{\text{enc}}^{(l)} \otimes A_{\text{sparse}}^{(l)}, \quad (12)$$

where \otimes represents a weighted operation applied to each channel.

After $F_{\text{sparse}}^{(l)'}$ undergoes the same decoding process as the dense prompt branch, it is transformed in size to obtain the sparse prompt embedding $P_s^{(c)}$. This embedding provides global features related to the class prompt. Combined with $P_d^{(c)}$, it meets the requirements of the mask decoder, thereby improving the quality of the generated mask.

C. Uncertainty-aware Joint Optimization

AutoMedSAM is designed to accommodate various modalities of medical images, which often have significant differences. Moreover, medical images generally have characteristics such as low contrast and high similarity among targets. To enhance segmentation accuracy, the model’s optimization process needs to integrate multiple loss functions to improve overall performance. However, as the number of loss functions increases, adjusting their weights becomes increasingly challenging, and these weights are crucial for model optimization as they directly influence the optimization direction [35]. To address this issue, we introduced a mechanism that incorporates uncertainty-aware into the loss weights setting, combining pixel-based, region-based, and distribution-based loss functions to evaluate the generated prompt embeddings and segmentation masks. By fully utilizing the complementary advantages of these loss functions, we assess and optimize model performance comprehensively. Specifically, we employed the following loss functions:

(1) Mean Squared Error (MSE) Loss: A pixel-based loss that focuses on the difference between predicted and true values for each pixel.

(2) Dice Coefficient (DC) Loss: A region-based metric that measures the overlap between the predicted region and the true region.

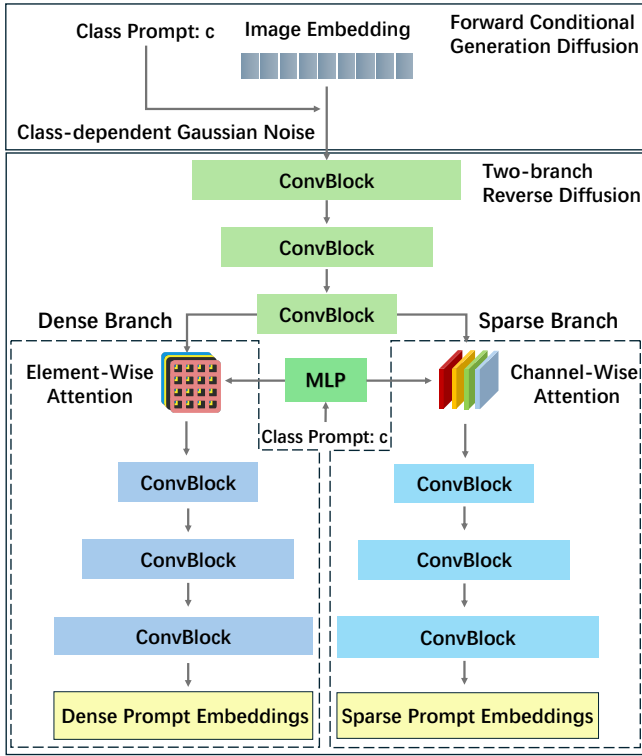


Fig. 3. Structure of the diffusion-based class prompt encoder. It is designed with an encoder and two independent decoder branches to extract local and global features, based on the practical significance of sparse and dense prompts. The use of prompt classes enables the model to more effectively focus on parts of the input related to specific classes, enhancing its ability to perceive and distinguish class-specific features, thereby improving the controllability and quality of the generation process.

(3) Cross-Entropy (CE) Loss: A distribution-based loss that focuses on the difference between the predicted probability distribution and the actual class distribution.

(4) Shape Distance (SD) Loss: A distribution-based loss that emphasizes the geometric and structural information of the target.

We first generate the sparse prompt embedding $P_{s,i}^{(c)}$ and dense prompt embedding $P_{d,i}^{(c)}$ using the original MedSAM prompt encoder and supervise the generation process of our diffusion-based class prompt encoder using MSE. This can be represented as:

$$L_{\text{MSE}^S} = \frac{1}{n} \sum_{c \in C} \sum_{i=1}^n (P_{s,i}^{(c)} - \hat{P}_{s,i}^{(c)})^2, \quad (13a)$$

$$L_{\text{MSE}^D} = \frac{1}{n} \sum_{c \in C} \sum_{i=1}^n (P_{d,i}^{(c)} - \hat{P}_{d,i}^{(c)})^2, \quad (13b)$$

where n represents the total number of samples, and C represents the set containing the prompted classes. In this way, our class prompt encoder can quickly leverage the extensive pre-trained knowledge from MedSAM’s original prompt encoder. For a given predicted mask and ground truth mask, we use the Dice Coefficient (DC) loss to evaluate their overlap, defined as:

$$L_{DC} = 1 - \frac{2 \sum_{c \in C} \sum_{i=1}^n M_i^{(c)} \hat{M}_i^{(c)}}{\sum_{c \in C} \left(\sum_{i=1}^n (M_i^{(c)})^2 + \sum_{i=1}^n (\hat{M}_i^{(c)})^2 \right)}. \quad (14)$$

Next, the classification probability for each pixel is evaluated using Cross-Entropy (CE) loss:

$$L_{CE} = -\frac{1}{n} \sum_{c \in C} \sum_{i=1}^n \left[M_i^{(c)} \log(\hat{M}_i^{(c)}) + (1 - M_i^{(c)}) \log(1 - \hat{M}_i^{(c)}) \right]. \quad (15)$$

For each channel ch of each sample, Shape Distance (SD) loss strengthens boundaries and shape consistency by calculating the average difference between the predicted result and the distance transform of the ground truth D . The calculation process of L_{SD} is as follows [36]:

$$f_{i,ch} = \frac{\sum_{h,w} |D(M_{i,ch}^{(c)}(h,w)) - M_{i,ch}^{(c)}(h,w)|}{\sum_{h,w} M_{i,ch}^{(c)}(h,w)}, \quad (16a)$$

$$L_{SD} = \frac{1}{n \cdot h} \sum_{i=1}^n \sum_{ch=1}^h f_{i,ch}. \quad (16b)$$

Finally, we combine all the losses through an uncertainty-aware framework. It is defined as:

$$L = \sum_{m=1}^M \left(\frac{1}{2\lambda_m^2} L_m + \log(1 + \lambda_m^2) \right), \quad (17)$$

where M represents the number of loss members involved in the optimization during training, L_m represents all the losses we mentioned above, and λ_m are learnable parameters that adjust the contribution of each loss component based on uncertainty.

IV. EXPERIMENT

A. Experimental Settings

1) Datasets: To evaluate the generalizability of AutoMedSAM, we conducted tests on several commonly used benchmark datasets, including AbdomenCT1K [37], BraTS [38], Kvasir-SEG [39], and Chest Xray Masks and Labels [40]. All data were obtained from the CVPR 2024 Medical Image Segmentation on Laptop Challenge¹. These datasets encompass four distinct imaging modalities: CT, MR, endoscopy, and X-ray, covering diverse segmentation targets ranging from organs to lesions. This diversity effectively demonstrates the broad applicability of our method. To equip the model for handling multimodal data, 3D images are converted into a three-channel format via slicing. Table I provides an overview of the datasets used.

TABLE I
DESCRIPTION OF THE DATASET USED IN THIS PAPER.

Dataset Name	Modality	Segmentation Targets
AbdomenCT-1K [37]	CT(3D)	Liver, kidneys, pancreas, spleen
BraTS [38]	MR-FLAIR(3D)	Brain tumor
Kvasir [39]	Endoscopy(2D)	Polyp
Chest Xray Masks and Labels [40]	Chest X-Ray(2D)	Lung

¹<https://www.codabench.org/competitions/1847>

TABLE II

COMPARATIVE RESULTS ON THE ABDOMENCT-1K DATASET. THE SAM-CORE MODEL RETAINS THE FOUNDATIONAL FRAMEWORK OF SAM, REQUIRING MANUAL PROMPTING FOR OPERATION. THE SAM-BASED MODEL BUILDS UPON SAM, INTRODUCING ENHANCEMENTS THAT ELIMINATE THE NEED FOR MANUAL PROMPTING. L. AND R. STAND FOR LEFT AND RIGHT. \uparrow MEANS HIGHER IS BETTER. *Italic* INDICATES THE BEST IN SAM-CORE MODEL, **BOLD** THE BEST IN SAM-BASED MODELS, AND UNDERLINE THE GLOBAL BEST.

Method Category	Method	DSC(%) \uparrow	NSD(%) \uparrow	Organ									
				DSC(%) \uparrow					NSD(%) \uparrow				
				Liver	Spleen	Pancreas	L.Kidney	R. Kidney	Liver	Spleen	Pancreas	L. Kidney	R. Kidney
SAM-Core Model	SAM [10]	89.79	83.94	92.117	93.766	72.694	95.254	95.121	75.376	90.253	69.687	92.385	91.998
	SAM2 [41]	90.191	85.137	93.815	95.391	70.793	95.623	95.334	81.804	94.149	62.519	93.86	93.354
	MedSAM [13]	<i>93.505</i>	<i>92.969</i>	<i>96.836</i>	<i>97.12</i>	<i>81.648</i>	<i>96.121</i>	<i>95.8</i>	<i>91.908</i>	<i>98.807</i>	<i>83.845</i>	<i>95.374</i>	<i>94.913</i>
	Med2d [42]	83.84	79.347	93.562	93.371	58.168	87.081	87.02	80.02	89.751	67.776	79.624	79.566
	U-MedSAM [43]	92.979	91.158	96.606	96.799	79.841	95.906	95.742	90.469	98.327	76.932	95.258	94.804
SAM-Based model	SAMed [44]	81.329	78.504	97.132	96.838	76.512	67.904	68.259	92.435	95.39	77.635	63.342	63.716
	H-SAM [45]	83.018	78.852	96.678	96.447	77.337	71.856	72.774	91.641	95.392	78.946	63.894	64.388
	AutoSAM [46]	82.258	76.305	96.326	95.625	72.555	73.206	73.578	89.899	91.574	72.391	63.589	64.073
	SurgicalSAM [16]	75.505	70.119	96.054	94.255	75.621	54.915	56.683	87.399	92.303	73.985	48.386	48.524
	AutoMedSAM(Ours)	94.58	95.148	97.467	96.958	86.061	96.291	96.121	95.03	98.911	88.903	96.585	96.309

2) *Evaluation Metrics*: To quantitatively evaluate the segmentation results, we adopted the Dice Similarity Coefficient (DSC) and Normalized Surface Distance (NSD) [13]. The DSC is a region-based metric used to evaluate the degree of overlap between the predicted segmentation mask and the expert annotation mask. It is defined as:

$$DSC(G, S) = \frac{2|G \cap S|}{|G| + |S|}, \quad (18)$$

where G and S denote the ground truth mask and the predicted segmentation mask, respectively.

The NSD is a boundary-based metric that measures the agreement between the boundaries of the predicted segmentation and the expert annotation, considering a specified tolerance τ . It is defined as:

$$NSD(G, S) = \frac{|\partial G \cap B_{\partial S}^{\tau}| + |\partial S \cap B_{\partial G}^{\tau}|}{|\partial G| + |\partial S|}, \quad (19)$$

where $B_{\partial G}^{\tau}$ and $B_{\partial S}^{\tau}$ denote the border regions around the boundaries of the ground truth and the predicted mask, respectively, within the tolerance τ . In evaluation, we set the tolerance τ to 2. For both metrics, a value approaching 1 represents superior segmentation performance, highlighting accurate spatial overlap and boundary consistency with the ground truth annotations.

3) *Efficient Tuning*: AutoMedSAM demonstrates high training efficiency by employing a selective tuning strategy. During the tuning phase, the large image encoder is kept frozen, while only the diffusion-based prompt encoder and mask decoder parameters are updated. This end-to-end tuning process is conducted under the supervision of the objective defined in (17), ensuring efficient optimization of the relevant components.

4) *Implementation Details*: All experiments were conducted using PyTorch and trained on an NVIDIA RTX A40 GPU. We set the batch size to 16 during training and trained for 100 epochs. The training process utilized the AdamW optimizer with a learning rate of $lr = 5 \times 10^{-4}$. The optimizer employed hyperparameters $\beta_1 = 0.9$, $\beta_2 = 0.999$, $\epsilon = 10^{-8}$. Additionally, a learning rate scheduler was used to reduce the learning rate on a plateau with a factor of 0.9, patience of 5 epochs, and no cooldown period.

5) *Baseline Methods*: We compared our method with state-of-the-art medical imaging SAM models, grouped into

SAM-Core models (SAM [10], SAM2 [41], MedSAM [13], Med2d [42], and U-MedSAM [43]) and SAM-Based models (SAMed [44], H-SAM [45], AutoSAM [46], and SurgicalSAM [16]). The SAM-Core Model retains the foundational framework of SAM, requiring manual prompting for operation. The SAM-Based Model builds upon SAM, introducing enhancements that eliminate the need for manual prompting. Notably, SurgicalSAM, like our approach, uses class prompts and prototype contrastive learning to distinguish surgical instruments. To ensure the reliability of the experimental results, all methods were conducted under identical experimental conditions.

B. Comparing with the Existing Methods

Prompt-based models should demonstrate the ability to identify multiple medical targets. Accordingly, we first evaluated the performance of various models on the multi-organ segmentation task using the AbdomenCT1K dataset. The experimental results are shown in Table II. It is evident that the proposed AutoMedSAM significantly outperforms other models, achieving average DSC and NSD scores of 94.58% and 95.148%, respectively, which are improvements of 1.075% and 2.511% over the second-best MedSAM. Moreover, except for the spleen, AutoMedSAM achieved the best results across all organs, with DSC and NSD scores exceeding those of the lowest-performing SurgicalSAM by 19.075% and 25.029%, respectively. These findings demonstrate the clear superiority of AutoMedSAM in multi-organ segmentation for medical applications. Further analysis shows that SAM-Core models outperform SAM-Based models on average. Among SAM-Core models, even the lowest-performing Med2D outperforms all SAM-Based models except for our proposed model. This difference is mainly attributable to SAM-Core models employing manual prompt mechanisms, which provide precise positional information, enabling the model to focus more effectively and deliver stable performance.

As shown in Table II, the segmentation performance of the tested models varies minimally for the liver, spleen, and pancreas but significantly deteriorates for kidney segmentation. To investigate this, we visualized the segmentation results (Fig. 4). Subfigures (a) and (b) in Fig. 4 illustrate that while SAM-Based models generally perform well in boundary recognition, they confuse the left and right kidneys. This is why their

performance drops sharply. However, during manual prompting, bounding boxes may unavoidably include other organs. Since SAM-Core models lack semantic information during prediction, they cannot accurately identify specific organs, leading to segmentation errors. As shown in subfigures (c) and (d) of Fig. 4, both SAM and MedSAM mistakenly identified other tissues to varying degrees. Additionally, even with minimal redundancy within bounding boxes, SAM models tend to segment features that appear prominent, which degrades mask quality (Fig. 4, subfigures (e) and (f)). In contrast, our method incorporates class-based prompts to introduce semantic information into predictions, effectively mitigating this issue.

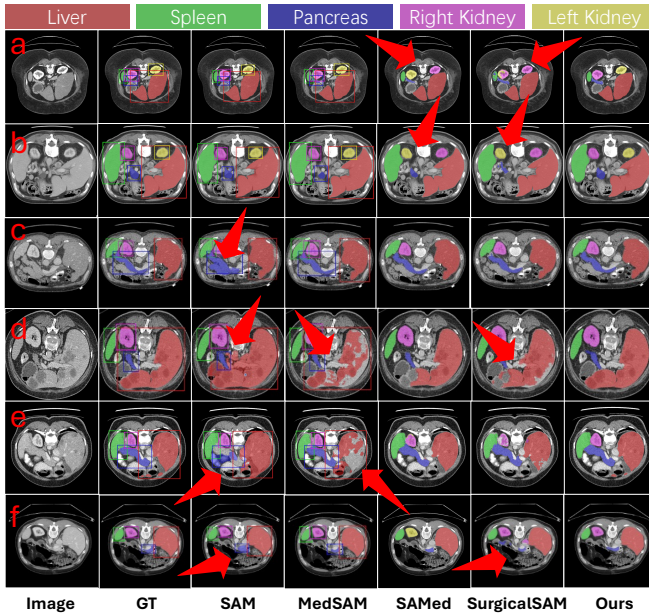


Fig. 4. The qualitative results of AutoMedSAM and other comparison models on AbdomenCT-1K. The bounding box represents the input prompt.

To evaluate segmentation accuracy independently, we conducted additional experiments on the BraTS, Kvasir-SEG, and Chest Xray Masks and Labels datasets. In BraTS and Kvasir-SEG, the targets (tumor and polyp) are singular but structurally complex, with diverse shapes and ambiguous boundaries. In Chest Xray Masks and Labels, overlapping structures like ribs around the lungs and the large target area introduce significant challenges. These datasets provide diverse difficulties suitable for evaluating segmentation performance. The results and visualizations are shown in Table III and Fig. 5, respectively.

As shown in Table III, AutoMedSAM achieved superior performance across all tasks, with DSC and NSD scores of 96.828% and 98.729% for polyp segmentation, demonstrating its adaptability to complex medical environments. Conversely, when SAM-Core models lose their advantage of manual prompts, their performance declines significantly. For example, in BraTS, SAM achieved only 69.667% DSC and 42.112% NSD for tumor segmentation, indicating reasonable overlap with ground truth but poor boundary recognition. Similar issues were observed in lung segmentation, as shown

in the last two subfigures of Fig. 5, where SAM models produced masks containing excessive non-target tissues. Finally, although SurgicalSAM also uses class-based prompts, its prototype-based contrastive learning framework reduces its adaptability in low-contrast, indistinct-boundary medical segmentation scenarios, limiting its ability to produce high-quality masks. In conclusion, the experimental results confirm that the proposed AutoMedSAM effectively adapts to various medical modalities, delivering accurate segmentation masks and achieving the best metrics across all datasets.

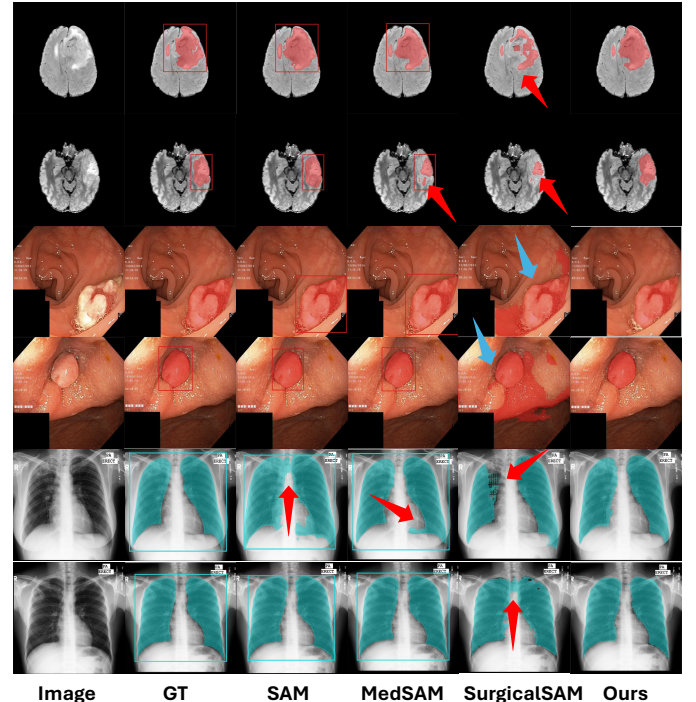


Fig. 5. The qualitative analysis results of AutoMedSAM and other comparison models on BraTS, Kvasir-SEG, and Chest Xray Masks and Labels.

C. Ablation Study

1) *Effects of Components in AutoMedSAM*: We conducted systematic ablation experiments on the Chest Xray Masks and Labels dataset to evaluate the specific contribution of each component to the method’s performance. As shown in Table IV, removing different components led to varying degrees of performance degradation. When both diffusion processing and uncertainty-aware joint optimization were excluded from the training process, the DSC and NSD of the model dropped to 88.62% and 89.19%, respectively, approximately a 7% decrease compared to the complete model, indicating the significant importance of these two components. Further analysis revealed that the absence of either component alone also caused substantial performance degradation. Additionally, removing the MSE loss and the pre-trained knowledge transferred from MedSAM (used to assist in training the diffusion-based class prompt encoder) had the second most significant impact on performance after the exclusion of diffusion processing or joint optimization. Finally, the absence of other components also led

TABLE III
COMPARATIVE RESULTS ON THE BRATS, KVASIR-SEG AND CHEST XRAY MASKS AND LABELS DATASETS

Method Category	Method	Dataset(Lesion/Organ)					
		BraTS(Tumor)		Kvasir-SEG(Polyp)		Chest Xray Masks and Labels(Lung)	
		DSC(%) \uparrow	NSD(%) \uparrow	DSC(%) \uparrow	NSD(%) \uparrow	DSC(%) \uparrow	NSD(%) \uparrow
SAM-Core Model	SAM [10]	69.667	42.112	92.749	95.384	94.326	94.878
	SAM2 [41]	77.061	57.808	94.013	96.282	95.423	95.975
	MedSAM [13]	89.568	89.517	95.803	97.829	95.864	96.354
	Med2d [42]	63.327	73.528	81.609	87.202	92.805	93.412
	U-MedSAM [43]	89.616	88.793	95.007	97.091	96.813	97.31
SAM-Based model	SAMed [44]	89.902	89.097	86.393	88.255	94.066	94.6
	H-SAM [45]	90.615	90.288	88.01	90.084	92.264	92.978
	AutoSAM [46]	90.24	89.186	87.045	89.288	89.616	90.516
	SurgicalSAM [16]	80.373	75.654	78.831	80.684	91.406	92.063
	AutoMedSAM(Ours)	91.057	92.661	96.828	98.729	96.941	97.367

to varying degrees of performance reduction. In conclusion, optimal segmentation performance can only be achieved by incorporating all components during training.

TABLE IV
ABLATION STUDY ON DIFFERENT COMPONENTS DURING AUTOMEDSAM TRAINING. THE GRAY ROW REPRESENTS OUR METHOD.

Diffusion Processing	Joint Optimization	CE	Dice	SD	MSE	DSC(%) \uparrow	NSD(%) \uparrow
✓	✓	✓	✓	✓	✓	92.573	93.281
✓	✓	✓	✓	✗	✓	95.263	95.8
✓	✓	✓	✗	✓	✓	94.452	95.208
✓	✓	✗	✓	✓	✓	93.57	94.06
✓	✗	✓	✓	✓	✓	93.359	94.113
✗	✓	✓	✓	✓	✓	91.562	92.194
✗	✗	✓	✓	✓	✓	88.62	89.19
✓	✓	✓	✓	✓	✓	96.941	97.367

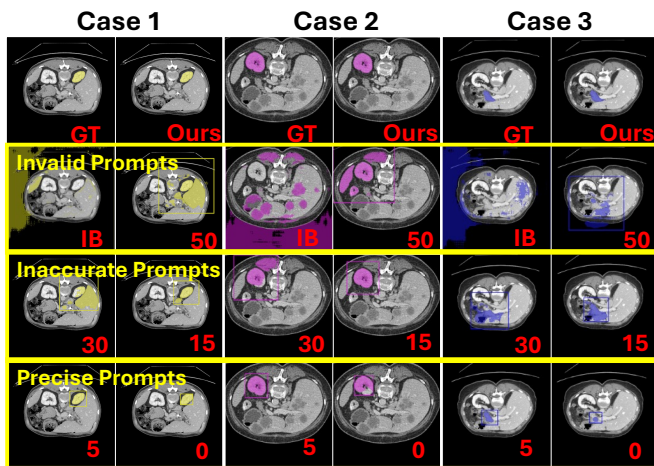


Fig. 6. The effect of different sized prompt boxes on segmentation masks. The marked numbers indicate the offset pixel size of the prompt box. IB represents the image boundary.

2) *Limitations of Manual Prompts*: As discussed in Sec. I, manually defined prompt boxes significantly constrain the segmentation accuracy of the model. To further investigate this phenomenon, we examined the impact of prompt boxes with varying offsets on the segmentation results. The experimental results, shown in Table V, indicate that segmentation accuracy improves as the boundaries of the prompt box approach the target object. However, the accuracy is not the best when the box aligns perfectly with the target boundary. Fig. 6 illustrates the segmentation masks under different prompt box configurations. The figure reveals that overly large prompt boxes include

multiple segmentable objects, leading to misidentification by the SAM-core model, as it struggles to determine the specific organ to segment. Conversely, overly small prompt boxes drive the model to search for deeper internal differences within the box, which reduces segmentation accuracy. To address these challenges, we proposed the class prompt method, which incorporates semantic information into the segmentation process. This approach eliminates errors caused by unstable manual prompts, simplifies the segmentation procedure, and enhances the model's robustness.

TABLE V
THE IMPACT OF BOUNDARY BOX PROMPTS WITH DIFFERENT ACCURACIES ON MEDSAM PERFORMANCE. THE EXPERIMENTAL RESULTS WERE TESTED ON THE ABDOMENCT1K DATASET.

Box Offset(pixel)	DSC(%) \uparrow	NSD(%) \uparrow
0	91.301	89.816
5	93.505	92.969
15	81.714	64.624
30	48.31	28.924
50	24.432	16.525
Image Boundary	2.359	2.366

V. CONCLUSION

In this paper, we proposed AutoMedSAM, a fully automated SAM-based medical image segmentation solution that demonstrates high effectiveness. AutoMedSAM consists of three components: an image encoder, a diffusion-based class prompt encoder, and a mask decoder. The diffusion-based class prompt encoder extracts relevant information from the image embedding based on the prompted class, and through two separate decoder branches, generates sparse and dense prompt embeddings. This design eliminates the need for manual prompts and additional prompt generators, achieving an end-to-end workflow that enhances system robustness and broadens application scenarios and user groups. Additionally, we introduced an uncertainty-aware joint optimization process, enabling the model to adaptively determine the weights of different loss functions to improve generalization capability. During joint optimization, we supervise both intermediate processes and final outputs to transfer the extensive knowledge of MedSAM to AutoMedSAM effectively. These strategies not only improve training efficiency but also significantly enhance segmentation accuracy. However, our current method

has only been trained on the datasets mentioned in this paper, and it does not yet fully meet the precision segmentation requirements for all organs and lesions. In the future, we will explore more lightweight solutions and further optimize the model on larger-scale medical datasets to enhance its practicality and applicability.

REFERENCES

- [1] R. Azad *et al.*, “Medical image segmentation review: The success of u-net,” *IEEE Trans. Pattern Anal. Mach. Intell.*, vol. 46, no. 12, pp. 10 076–10 095, 2024.
- [2] Z. Marinov, P. F. Jäger, J. Egger, J. Kleesiek, and R. Stiefelwagen, “Deep interactive segmentation of medical images: A systematic review and taxonomy,” *IEEE Trans. Pattern Anal. Mach. Intell.*, vol. 46, no. 12, pp. 10 998–11 018, 2024.
- [3] P. Huang, S. Hu, B. Peng, J. Zhang, X. Wu, and X. Wang, “Robustly optimized deep feature decoupling network for fatty liver diseases detection,” in *Proc. Int. Conf. Med. Image Comput. Comput.-Assist. Intervent. (MICCAI)*. Springer, 2024, pp. 68–78.
- [4] X. Wang and H. Zhu, “Artificial intelligence in image-based cardiovascular disease analysis: A comprehensive survey and future outlook,” *arXiv:2402.03394*, 2024.
- [5] A. Hatamizadeh *et al.*, “Unetr: Transformers for 3d medical image segmentation,” in *Proc. IEEE/CVF Winter Conf. Appl. Comput. Vis. (WACV)*, Jan 2022.
- [6] J. Ma, F. Li, and B. Wang, “U-mamba: Enhancing long-range dependency for biomedical image segmentation,” *arXiv preprint arXiv:2401.04722*, 2024.
- [7] H.-Y. Zhou *et al.*, “nnformer: Volumetric medical image segmentation via a 3d transformer,” *IEEE Trans. Med. Imag.*, vol. 32, pp. 4036–4045, 2023.
- [8] K. Weiss, T. M. Khoshgoftaar, and D. Wang, “A survey of transfer learning,” *J. Big Data*, vol. 3, pp. 1–40, 2016.
- [9] A. Hosna, E. Merry, J. Gyalmo, Z. Alom, Z. Aung, and M. A. Azim, “Transfer learning: a friendly introduction,” *J. Big Data*, vol. 9, no. 1, p. 102, 2022.
- [10] A. Kirillov *et al.*, “Segment anything,” in *Proc. IEEE Int. Conf. Comput. Vis. (ICCV)*, 2023, pp. 4015–4026.
- [11] C. Zhang *et al.*, “A comprehensive survey on segment anything model for vision and beyond,” *arXiv preprint arXiv:2305.08196*, 2023.
- [12] N. Zhou *et al.*, “Medsam-u: Uncertainty-guided auto multi-prompt adaptation for reliable medsam,” *arXiv preprint arXiv:2409.00924*, 2024.
- [13] J. Ma, Y. He, F. Li, L. Han, C. You, and B. Wang, “Segment anything in medical images,” *Nat. Commun.*, vol. 15, no. 1, p. 654, 2024.
- [14] Y. Zhang and R. Jiao, “Towards segment anything model (sam) for medical image segmentation: a survey,” *arXiv preprint arXiv:2305.03678*, 2023.
- [15] C. Li, P. Khanduri, Y. Qiang, R. I. Sultan, I. Chetty, and D. Zhu, “Autoprosam: Automated prompting sam for 3d multi-organ segmentation,” *arXiv preprint arXiv:2308.14936*, 2023.
- [16] W. Yue, J. Zhang, K. Hu, Y. Xia, J. Luo, and Z. Wang, “Surgicalsam: Efficient class promptable surgical instrument segmentation,” in *Proc. AAAI Conf. Artif. Intell.*, vol. 38, 2024, pp. 6890–6898.
- [17] B. Xie, H. Tang, B. Duan, D. Cai, and Y. Yan, “Masksam: Towards auto-prompt sam with mask classification for medical image segmentation,” *arXiv preprint arXiv:2403.14103*, 2024.
- [18] M. A. Mazurowski, H. Dong, H. Gu, J. Yang, N. Konz, and Y. Zhang, “Segment anything model for medical image analysis: An experimental study,” *Med. Image Anal.*, vol. 89, p. 102918, 2023.
- [19] Y. Zhang, Z. Shen, and R. Jiao, “Segment anything model for medical image segmentation: Current applications and future directions,” *Comput. Biol. Med.*, vol. 171, p. 108238, 2024.
- [20] B.-H. Le, D.-K. Nguyen-Vu, T.-H. Nguyen-Mau, H.-D. Nguyen, and M.-T. Tran, “Medficientsam: A robust medical segmentation model with optimized inference pipeline for limited clinical settings,” in *CVPR 2024: Segment Anything In Medical Images On Laptop*, 2024.
- [21] X. Zhang, Y. Liu, Y. Lin, Q. Liao, and Y. Li, “Uv-sam: Adapting segment anything model for urban village identification,” in *Proc. AAAI Conf. Artif. Intell.*, vol. 38, 2024, pp. 22 520–22 528.
- [22] J. N. Paranjape, N. G. Nair, S. Sikder, S. S. Vedula, and V. M. Patel, “Adaptivesam: Towards efficient tuning of sam for surgical scene segmentation,” in *Proc. Conf. Med. Image Underst. Anal. (MIUA)*. Springer, 2024, pp. 187–201.
- [23] W. Yue *et al.*, “Part to whole: Collaborative prompting for surgical instrument segmentation,” *arXiv preprint arXiv:2312.14481*, 2023.
- [24] P. Yan, M. Li, J. Zhang, G. Li, Y. Jiang, and H. Luo, “Cold segdiffusion: A novel diffusion model for medical image segmentation,” *Knowl.-Based Syst.*, vol. 301, p. 112350, 2024.
- [25] Z. Zhu, Y. Liu, C.-A. Yuan, X. Qin, and F. Yang, “A diffusion model multi-scale feature fusion network for imbalanced medical image classification research,” *Comput. Meth. Prog. Bio.*, vol. 256, p. 108384, 2024.
- [26] A. Fontanella, G. Mair, J. Wardlaw, E. Trucco, and A. Storkey, “Diffusion models for counterfactual generation and anomaly detection in brain images,” *IEEE Trans. Med. Imag.*, 2024.
- [27] A. Kazerouni *et al.*, “Diffusion models in medical imaging: A comprehensive survey,” *Med. Image Anal.*, vol. 88, p. 102846, 2023.
- [28] M. Usman Akbar, M. Larsson, I. Blystad, and A. Eklund, “Brain tumor segmentation using synthetic mr images—a comparison of gans and diffusion models,” *Sci. Data*, vol. 11, no. 1, p. 259, 2024.
- [29] D. Stojanovski, M. da Silva, P. Lamata, A. Beqiri, and A. Gomez, “Efficient semantic diffusion architectures for model training on synthetic echocardiograms,” *arXiv preprint arXiv:2409.19371*, 2024.
- [30] Y. Luo *et al.*, “Target-guided diffusion models for unpaired cross-modality medical image translation,” *IEEE J. Biomed. Health Inform.*, 2024.
- [31] S. Pan *et al.*, “Synthetic ct generation from mri using 3d transformer-based denoising diffusion model,” *Med. Phys.*, vol. 51, no. 4, pp. 2538–2548, 2024.
- [32] S. Ramanarayanan, A. Sarkar, M. N. Gayathri, K. Ram, M. Sivaprakasam *et al.*, “Dce-diff: Diffusion model for synthesis of early and late dynamic contrast-enhanced mr images from non-contrast multimodal inputs,” in *Proc. IEEE/CVF Conf. Comput. Vis. Pattern Recognit. (CVPR)*, 2024, pp. 5174–5183.
- [33] O. Ronneberger, P. Fischer, and T. Brox, “U-net: Convolutional networks for biomedical image segmentation,” in *Proc. Int. Conf. Med. Image Comput. Comput.-Assist. Intervent. (MICCAI)*. Springer, 2015, pp. 234–241.
- [34] Z. Wu, C. Shen, and A. Van Den Hengel, “Wider or deeper: Revisiting the resnet model for visual recognition,” *Pattern Recogn.*, vol. 90, pp. 119–133, 2019.
- [35] T. Y. Tsai, L. Lin, S. Hu, M.-C. Chang, H. Zhu, and X. Wang, “Uu-mamba: Uncertainty-aware u-mamba for cardiac image segmentation,” in *IEEE Int. Conf. Multimed. Inf. Process. Retrieval (MIPR)*, 2024, pp. 267–273.
- [36] Q. Huang, Y. Zhou, and L. Tao, “Dual-term loss function for shape-aware medical image segmentation,” in *Proc. IEEE Int. Symp. Biomed. Imaging (ISBI)*, 2021, pp. 1798–1802.
- [37] J. Ma *et al.*, “Abdomenct-1k: Is abdominal organ segmentation a solved problem?” *IEEE Trans. Pattern Anal. Mach. Intell.*, vol. 44, no. 10, pp. 6695–6714, 2021.
- [38] B. H. Menze *et al.*, “The multimodal brain tumor image segmentation benchmark (brats),” *IEEE Trans. Med. Imag.*, vol. 34, no. 10, pp. 1993–2024, 2014.
- [39] D. Jha *et al.*, “Kvasir-seg: A segmented polyp dataset,” in *Proc. Int. Conf. MultiMedia Model. (MMM)*. Springer, 2020, pp. 451–462.
- [40] S. Candemir *et al.*, “Lung segmentation in chest radiographs using anatomical atlases with nonrigid registration,” *IEEE Trans. Med. Imag.*, vol. 33, no. 2, pp. 577–590, 2013.
- [41] N. Ravi *et al.*, “Sam 2: Segment anything in images and videos,” *arXiv preprint arXiv:2408.00714*, 2024.
- [42] J. Cheng *et al.*, “Sam-med2d,” *arXiv preprint arXiv:2308.16184*, 2023.
- [43] X. Wang, X. Liu, P. Huang, P. Huang, S. Hu, and H. Zhu, “U-medsam: Uncertainty-aware medsam for medical image segmentation,” *arXiv preprint arXiv:2408.08881*, 2024.
- [44] K. Zhang and D. Liu, “Customized segment anything model for medical image segmentation,” *arXiv preprint arXiv:2304.13785*, 2023.
- [45] Z. Cheng *et al.*, “Unleashing the potential of sam for medical adaptation via hierarchical decoding,” in *Proc. IEEE/CVF Conf. Comput. Vis. Pattern Recognit. (CVPR)*, 2024, pp. 3511–3522.
- [46] X. Hu, X. Xu, and Y. Shi, “How to efficiently adapt large segmentation model (sam) to medical images,” *arXiv preprint arXiv:2306.13731*, 2023.